ELSEVIER

Journal of Structural Geology 28 (2006) 408–420

JOURNAL OF STRUCTURAL GEOLOGY

www.elsevier.com/locate/jsg

Rapid digital quantification of microfracture populations

Leonel A. Gomez [a,b,*], Stephen E. Laubach [b]

[a] Department of Geological Sciences, Jackson School of Geosciences, The University of Texas at Austin, Austin, TX, USA
[b] Bureau of Economic Geology, Jackson School of Geosciences, The University of Texas at Austin, Austin, TX, USA

Received 30 March 2005; received in revised form 28 November 2005; accepted 2 December 2005

Abstract

Populations of microfractures are a structural fabric in many rocks deformed at upper crustal conditions. In some cases these fractures are visible in transmitted-light microscopy as fluid-inclusion planes or cement filled microfractures, but because SEM-based cathodoluminescence (CL) reveals more fractures and delineates their shapes, sizes, and crosscutting relations, it is a more effective structural tool. Yet at magnifications of 150–300×, at which many microfractures are visible, SEM-CL detectors image only small sample areas (0.5–0.1 mm^2) relative to fracture population patterns. The substantial effort required to image and measure centimeter-size areas at high-magnification has impeded quantitative study of microfractures. We present a method for efficient collection of mosaics of high-resolution CL imagery, a preparation method that allows samples to be any size while retaining continuous imagery of rock (no gaps), and software that facilitates fracture mapping and data reduction. Although the method introduced here was developed for CL imagery, it can be used with any other kind of images, including mosaics from petrographic microscopes. Compared with manual measurements, the new method increases several fold the number of microfractures imaged without a proportional increase in level of effort, increases the accuracy and repeatability of fracture measurements, and speeds quantification and display of fracture population attributes. We illustrate the method on microfracture arrays in dolostone from NE Mexico and sandstone from NW Scotland. We show that key aspects of microfracture population attributes are only fully manifest at scales larger than a single thin section.

Keywords: Aperture; Dolostone; Fluid-inclusion plane; Sandstone; Scaling; Spacing

1. Introduction

Observation of structural fabrics on the millimeter to centimeter scale is a central technique in structural analysis. In many tectonites, light or scanning-electron (SEM) microscopy at the thin-section scale produces useful results. Examples include many types of cleavage and certain fault fabrics. For these rocks, the size of a meaningful fabric sample is small compared with the size of the rock volume available within a single thin section. Although the size of an individual element of a structural fabric (e.g. one gouge particle, one microfracture) is typically smaller than the rock available within a single thin section, quantitative studies of fabrics sometimes requires measurement having at least one dimension (length or width) larger than an individual thin section. In these cases, and where time-consuming measurements at high resolution over large areas are required for meaningful analysis, machine-assisted workflows are increasingly used. An example is documentation of crystallographic preferred orientation patterns (van Daalen et al., 1999). We define microfracture as a fracture that can only be detected with magnification (Laubach, 1997).

Microfractures are a widespread but underutilized structural fabric. They can be used as paleostress indicators (Laubach, 1989; Lespinasse, 1999), strain gauges, and markers of deformation timing (Laubach, 2003). In sedimentary rocks, description of microfracture populations that have been fossilized by authigenic cements is another type of analysis that involves time-consuming, high-magnification measurement (Laubach, 1997; Marrett et al., 1999; Ortega and Marrett, 2000). For example, in many sandstones quartz-sealed microfractures are visible using SEM-based cathodoluminescence (SEM-CL, Fig. 1b) but are invisible under petrographic microscopy (Milliken and Laubach, 2000; Laubach et al., 2004).

Owing to the configuration of most SEM-CL detectors (Kearsley and Wright, 1988), an individual image at the requisite magnification is a minute fraction of the area of a typical thin section (e.g. about 0.3 mm^2, or 0.01% of the typical

* Corresponding author. Department of Geological Sciences, Jackson School of Geosciences, The University of Texas at Austin, Austin, TX, USA. Tel.: +1 512 478 2879.
E-mail addresses: leonelgomez@mail.utexas.edu; leonelgomeztorres@yahoo.com (L.A. Gomez).

0191-8141/$ - see front matter © 2006 Elsevier Ltd. All rights reserved.
doi:10.1016/j.jsg.2005.12.006

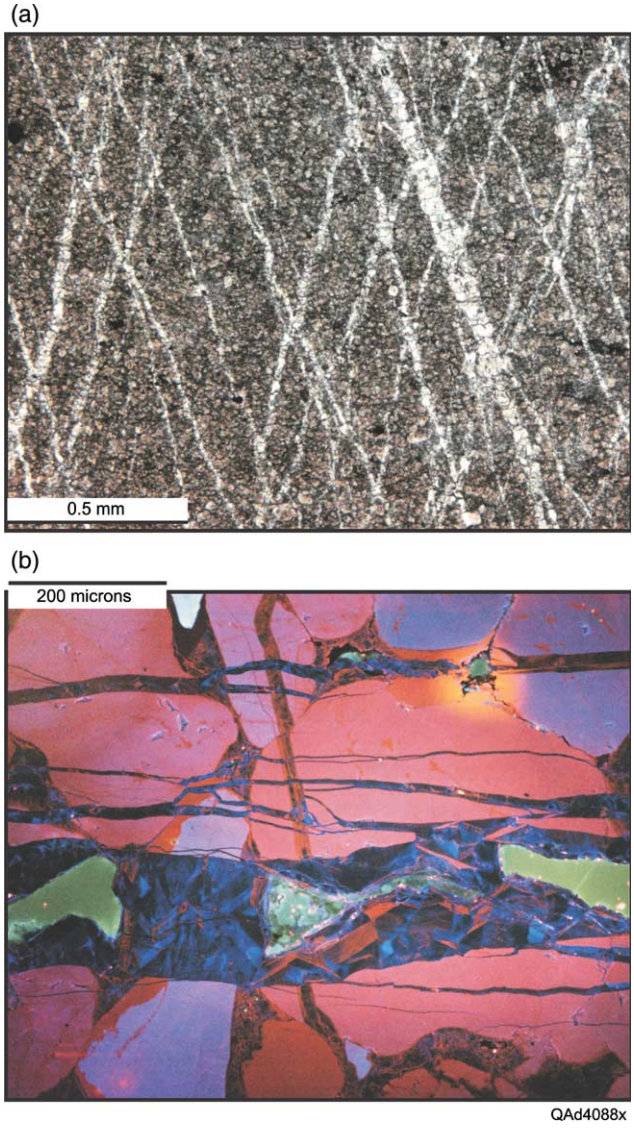

Fig. 1. Photomicrographs and SEM-CL images of microfractures. (a) Transmitted-light image of microfractures in Cretaceous Cupido dolostone, Mexico. Fractures are lined with dolomite and filled with calcite and show mutually crosscutting relations. (b) Two sets of quartz-sealed microfractures, Cambrian Eriboll Formation sandstone, Dundonnell Bridge, Scotland. Early fractures (red quartz) are crosscut by later fractures (blue quartz). SEM-CL synthetic color from superposing multiple panchromatic CL images captured using red, green, and blue filters (image, R. Reed). In transmitted light, some microfractures are visible as fluid-inclusion planes.

amount of rock in a 50×75-mm-thin section at a magnification of 200×). Yet for fracture patterns and population statistics to be adequately documented, image areas of cm^2 are commonly required (Gomez et al., 2003). Clearly a machine-assisted workflow is needed for effective collection and processing of this type of structural fabric data over more than one thin section.

Here we illustrate a method of rapid digital quantification of microfracture populations consisting mostly of sample-preparation methods, software, and mapping procedures we developed but also involving adaptations of commercially available hardware and software. The workflow includes a new method of producing sequential thin sections along continuous rock traverses without gaps (missing rock) and that are suitable for use in SEMs. We take advantage of existing automation software for SEMs to create CL mosaics that are as long as the available sample. To map and measure fractures efficiently on images, we combine commercial digitizing software for mapping fractures and spreadsheet-based software that we created for data reduction and analysis.

The method presented herein comprises four main steps. First, a thin section or polished slab is generated. If a continuous area larger than that of an individual thin section is desired, a suite of consecutive thin sections is prepared using a procedure described later. Second, images are acquired using software that drives an SEM stage. However, other types of imagery, including images collected using transmitted-light microscopes, can also be used. Third, we digitize microfractures using commercial digitizing software and export fracture coordinates to a spreadsheet. Fourth, our spreadsheet-based software quantifies and displays attributes of all or part of the fracture population. In this paper we describe each step, and then illustrate its application to microfracture arrays in dolostone from NE Mexico (petrographic imagery) and sandstone from NW Scotland (SEM-CL imagery). Our method makes microfracture analysis more accessible and effective. We show that key aspects of microfracture population attributes are only fully manifest at scales larger than a single thin section. Together with the scaling methods of Marrett et al. (1999), our results can be used for quantitative extrapolation of fracture attributes from fractures on a thin-section scale (microfractures) to larger scales (macrofractures).

2. Sample preparation and mosaic acquisition

The first step in microfracture analysis is preparation of suitable samples and subsequent thin sections. Because we are measuring fractures that are mostly filled with cement, no special handling designed to preserve or measure open fractures is needed (Kranz, 1983). The second step is to image the rock. For many applications, it involves collecting images at high magnification then stitching the images together into a mosaic. Although this is the rate-limiting step for the entire process, automated image collection can greatly reduce the researcher's time.

For one-dimensional (1-D) inventories of fracture populations, we measure fracture attributes along a line (commonly known as a scanline) normal to dominant fracture strike (Marrett, 1996). To accomplish such 1-D analysis, we acquire a strip of contiguous images and generate a long and narrow image mosaic. For two-dimensional (2-D) analysis and quantification of fracture length, an equidimensional mosaic is needed. Long, narrow image mosaics require less effort to create, but they are biased toward sampling fractures at a high angle to the scanline and commonly have censoring of fracture lengths. Nevertheless, if they are long enough to capture a representative population of fracture sizes, 1-D scanlines in thin sections can provide useful information on fracture strain, aperture scaling, orientation, and spacing (Marrett et al., 1999;

Gomez, 2004). The examples we present later are based on 1-D scanline analysis.

2.1. Consecutive thin sections

A special problem of 1-D analysis occurs when the desired scanline length is much longer than that of a single thin section. To properly study all microfractures in a sample larger than one thin section requires more than just several adjacent thin sections. It demands consecutive thin sections prepared in such a way that there is *no sample gap* between them.

There are at least three reasons why such large continuous samples are needed. First, in many rocks, the number of transgranular microfractures detected in a scanline across an individual thin section may not be large enough to generate a reliable cumulative frequency distribution of any fracture attribute (Gomez et al., 2003). For example, half of the samples of Gross and Engelder (1995) did not have enough microfractures to quantify the relative abundances of large and small fractures, expressed as the exponent of the power-law distribution of fracture apertures.

Second, gaps made during preparation of consecutive thin-sections can have systematic locations and vary widely in size. Gaps that are not randomly located can have effects on the statistics of the fracture population that are difficult to estimate or predict. Cumulative frequency distributions of fracture attributes such as aperture or spacing should be generated, with data measured along a *continuous* scanline or inside a *continuous* area (Marrett et al., 1999; Ortega and Marrett, 2000; Gillespie et al., 2001). Gaps can introduce errors into analysis of fracture spatial arrangement, particularly where fractures are clustered. For example, not knowing the exact size of the sample gap will introduce an inaccuracy in the scanline length; if fractures were present in that gap, their absence would also have an unpredictable impact on the fracture population.

Third, some fracture clusters are wider than the dimension of a single thin section. Therefore, only by accurately measuring the spacing between microfractures along groups of consecutive thin sections without sample gaps between them would it be possible to quantify the spatial arrangement of microfractures inside the cluster (Gomez, 2004).

Consequently, we developed a method outlined in Figs. 2 and 3 that allows the generation of consecutive thin sections of conventional size (currently as many as seven 50×75 mm) while eliminating loss of sample between sections caused by sawing during sectioning. To generate consecutive thin sections the first step is to obtain suitable rock samples that lack any breaks or discontinuities. The next step is to define the plane where the consecutive thin sections are going to be located and to cut the rock sample into a relatively thin (typically as much as 30 mm thick) slab parallel to that plane. Generally it is possible to define a plane that is approximately perpendicular in 3-D to most of the fractures belonging to the set under scrutiny (Fig. 2).

We preserve rock continuity between adjacent thin sections by modifying how the rock slab is separated into thin-section-size chips. This modification is accomplished by preventing the trim saw from cutting entirely across the slab (Figs. 2 and 3). By stopping the cut in the back of the sample (the side opposite to where the thin sections will be placed) a few millimeters before it crosses the slab, the sample can be broken using gentle pressure. The resulting rupture mostly preserves continuous rock, and continuity can be achieved with a little practice. Our newly developed method complements previous sample preparation methods (i.e. Chapter 10, Passchier and Trouw, 1998). Although in our experience, rock samples larger than one thin section have a better chance of properly quantifying a fracture population, in many instances there will not be sufficient sample, time, or resources to obtain a suite of consecutive thin sections. With the exception of how to prepare a suite of consecutive thin sections, all other methods presented herein are suitable for individual thin sections.

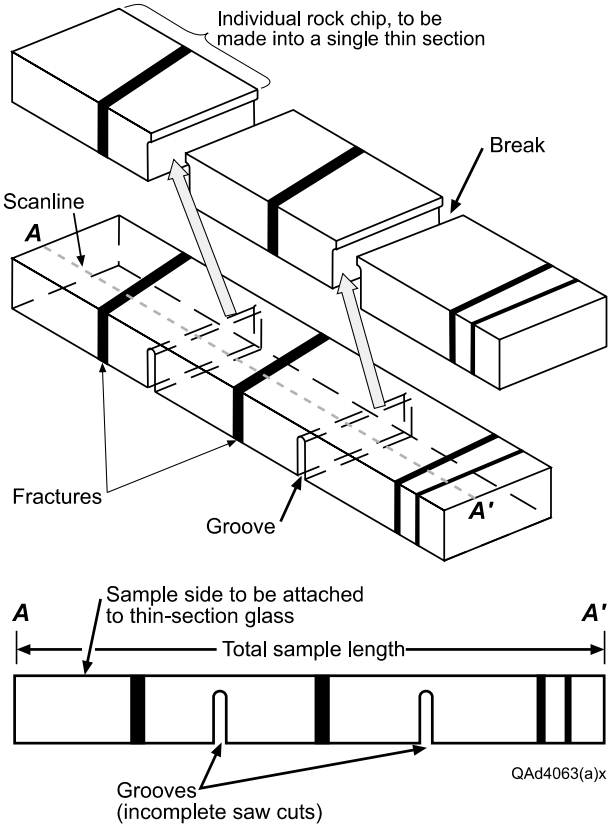

Fig. 2. Procedure for preparing consecutive thin sections having no sample gap between them. Long side of rock slab is perpendicular to fractures (black lines). Middle (block diagram) and lower (cross-section) sketches show grooves (incomplete saw cuts, dashed lines) that stop short of crossing the slab. Upper sketch shows sample broken at grooves. Conventional thin-section preparation involves use of a trim saw (approximate kerf 1 mm) to cut slab into thin chips. All of these cuts remove material from between adjacent sections. Our technique preserves this material.

2.2. Transmitted-light imaging

In some rocks, cement-filled microfractures are readily visible using transmitted-light microscopy (Fig. 1a). The method we present can be applied to mosaic images generated using petrographic microscopes and a digital camera. We use

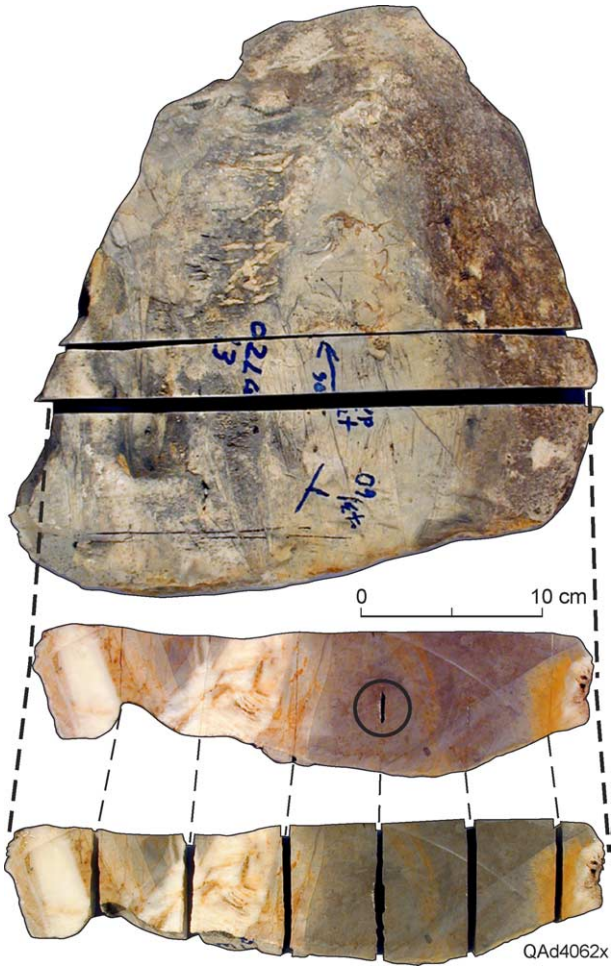

Fig. 3. Progression from intact sample to consecutive thin sections, Cupido dolostone. Top image shows excision of slab sample. Notice gaps caused by slab saw. Middle image shows rock slab on continuous sample face broken into seven contiguous chips. Incomplete saw cuts (dashed lines) are on opposite side of sample. Note rock continuity except area marked by circle that shows where a saw cut penetrated the continuous face, illustrating how much rock is lost owing to saw cuts. Lower image shows sample separated along incomplete saw cuts. If the rock sample is oriented, it is important to record the orientation of the rock slab and each thin section with respect to geographic north.

a graduated mechanical stage to make controlling the position of the thin section easier, facilitating alignment and proper overlap of individual images for image stitching. Having a digital or paper copy of an entire individual thin-section image helps register features on adjacent thin sections. The area of individual images typically varies between 5.5 (30×) and 0.3 (125×) mm^2, the equivalent of 0.24–0.01% of the rock available in a typical 50×75 mm thin section. Image collection using petrographic microscopes could be automated, but at typical magnifications used for microfracture quantification (30–125×), the number of images per thin section is small enough (around 30 images at 50× along 45 mm of sample) that the manual approach is practical. Such is not the case for most scanned-CL image mosaics, where as a result of the restricted field of view, at 200×, approximately 85 images would be required to cover the same length. Because rock usually does not extend to the edges of a thin section, those 45 mm could correspond to the scanline length along the short side of a typical 50×75 mm thin section.

2.3. SEM-based cathodoluminescence (SEM-CL)

SEM-CL imaging of microfractures is a useful structural technique because it delineates fracture shapes, sizes, and crosscutting relations that otherwise would be difficult or impossible to discern (Fig. 1b). Yet at 150–300×, where many fractures are visible, SEM-CL detectors image only small sample areas (0.5–0.1 mm^2—the equivalent of 0.02–0.003% of the rock available in a typical 50×75 mm thin section). This is a small area relative to fracture-population patterns, and the effort required to image a representative area of the sample at these magnifications impedes use of microfractures. Image collection and stage-control-automation software for SEMs helps remove this impediment.

Electron-beam-excited photons detected and used for CL microscopy reflect subtle chemical and structural differences (Pagel et al., 2000, and references therein). In quartz, for example, luminescence variations result from differences in trace-element composition and mineral structure. SEM-CL imaging allows detection of quartz-lined microfractures that are not readily visible using transmitted light or cold-cathode CL microscopy (Milliken and Laubach, 2000). Owing to the stable observing conditions, high magnifications, and sensitive light detection that characterize this detection method (Kearsley and Wright, 1988), SEM-CL permits rapid collection of images having higher resolution than those of conventional light-microscope-based CL systems.

Images in this study were acquired using an Oxford Instruments MonoCL2 system attached to a Philips XL30 SEM operating at 15 or 20 kV. Detectors and processing record CL emissions in the range of ultraviolet through visible into near infrared (185–850 nm) and convert them to gray-scale intensity values (Figs. 1b and 4). Apart from moving between image locations manual acquisition of a single SEM secondary electron image (SEI) takes about 2 min, whereas a single CL image takes between 3 (typical sandstone) and 6 min (typical carbonate rock). A mosaic of SEM images collected manually forces the operator to wait until one image is acquired, save that image, move the stage to its new position, and start collection of the contiguous image. It is a cumbersome process that makes poor use of the operator's time. The solution is automation of stage movement and image collection.

The SEM mosaics used in this study were collected using Oxford Instruments' Autostage software (part of its ISIS analytical and imaging system). We also collect image mosaics using Scandium® stage control and image collection, an SEM-specific version of analySIS software from Soft Imaging Systems Inc. This software guides both SEM stage and imaging system so that we can acquire consecutive digital images along a predetermined line (or other prescribed area) without subsequent operator input. The SEM user controls start point, end point, and distance between images. Sample geology and study objectives govern the optimal images area size

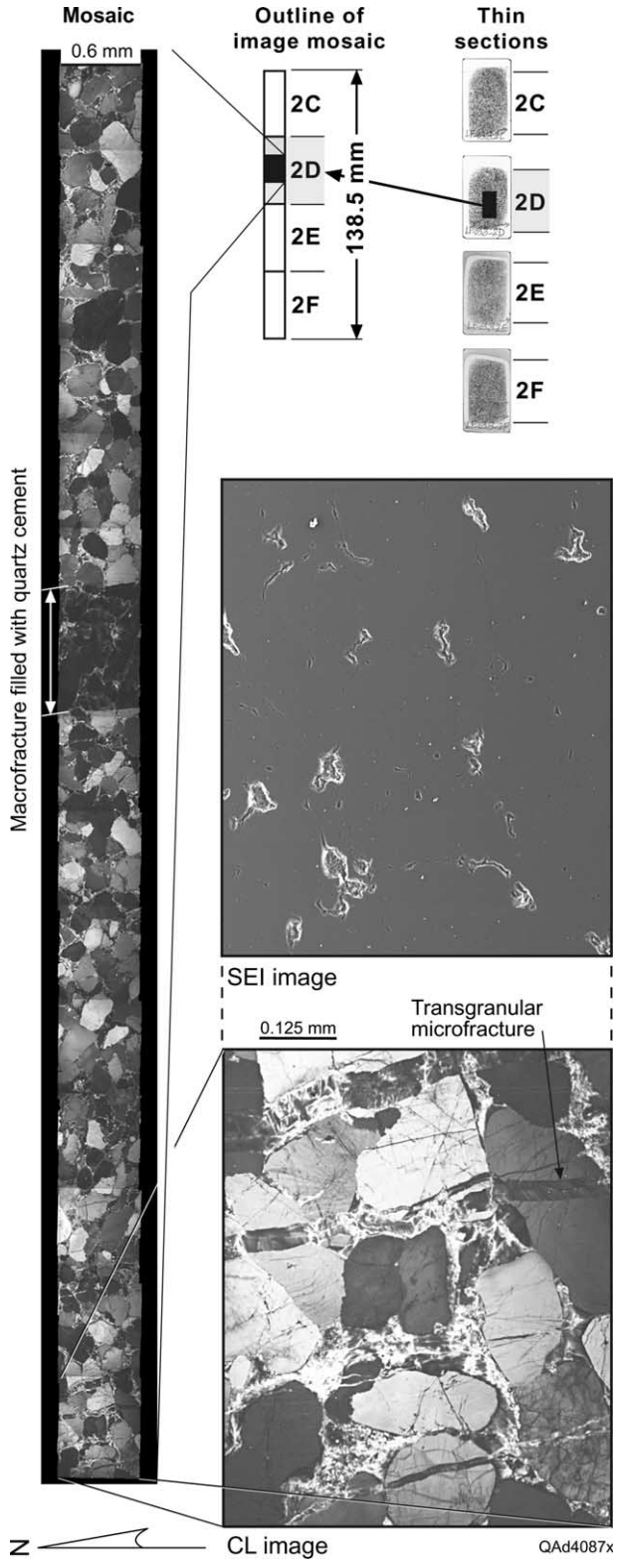

Fig. 4. Part of SEM-based CL mosaic from consecutive thin section suite of sandstone. Plane of section is parallel to bedding. Length of image mosaic shown covers about two-thirds of a 25×46 mm thin section. Entire CL mosaic is 138.5 mm long and was imaged at 150×. Expanded view shows an individual CL image and matching SEI image. Note transgranular, north-northwest-striking fractures. Inset shows area of image (box) compared with the area of four thin sections without gaps between them. Sample is Cambrian Eriboll Formation sandstone, near Lochan Fada, Wester Ross, Scotland (National grid reference: NH045704).

and shape. For example, in coarse sandstone we collect larger mosaics to encompass the larger grain size.

At a magnification of 200×, a distance between image centers of 530 microns allows for about 10% image overlap, which is needed to effectively stitch contiguous images in mosaics. Typically at least 10–15 images can be acquired in a single automatic run before focus is lost owing, mainly, to nonplanarity of imaged surface. At 200×, a scanline across the rock in a typical 50-mm-wide thin section (about 45 mm) would need 85 pairs of SEI and CL images, which would require about 10 h of SEM time but only about 2 h of SEM-operator time.

Without automation, generation of image mosaics larger than one thin section is prohibitive. It took about 32 h of SEM time but only 8 h of the operator's time to acquire SEI and CL images on the long dimension of four 25×46 mm thin sections (138.5 mm) of a quartz-cemented sandstone (Section 4.2) using SEM automation software. In contrast, manual acquisition of the same number of images would have taken at least the same number of hours of SEM time and effectively the same amount of SEM-operator time. Automation makes acquiring mosaic images that extend beyond a single thin section practical.

2.4. Mosaic stitching

Once individual images are collected from either a petrographic microscope or a SEM (Fig. 1) and adjusted to enhance structural features, they must be stitched into mosaics (Fig. 4), which can be done manually using image-editing software, such as Photoshop®, or image-stitching software, such as Panavue®. Because the electron beam causes changes in luminescence as CL images are acquired, auto-stitching programs may not match adjacent CL images accurately because of beam-induced luminescence differences in the image overlap zone. These luminescence variations may need to be adjusted manually. Some image-acquisition programs will also stitch images automatically, which is the procedure we currently use with Scandium® stage control and image collection. To facilitate manual stitching or to verify the accuracy of image mosaics stitched automatically, we recommend that each thin section be scanned in a single digital file. We co-register SEI and CL images in layered image files in order to better identify the location of pores on CL images (Fig. 4). This co-registration necessitates doubling the number of images collected per mosaic. Color imaging using filters increases threefold the number of CL images required. Although two orthogonal scale bars will facilitate the calibration of each image mosaic, one scale bar will suffice.

On the SEM, we used automated image collection systems to create mosaics at 150–300× that have areas of as much as 89 mm^2 (0.64×138.5 mm). Our largest mosaic of scanned CL contains 191 images (Section 4.2), but it documents only 2% of the rock available. On the petrographic microscope, we manually acquired long and narrow image mosaics (1-D analysis) at magnifications of 50× that have areas of as much as 388 mm^2 (1.4×277 mm). Our largest mosaic from transmitted-light microscopy contains 194 images

(Section 4.1), and it also documents only 2% of the rock available. These two long mosaics were derived from sequential thin sections prepared from consecutive thin-section suites having no gaps (Figs. 2 and 3).

3. Fracture-mapping procedure and quantification

The next steps in microfracture analysis are to map and quantify the microfracture attributes. Procedures for microfracture mapping must be capable of efficiently recording numerous microfracture attributes for thousands of fractures at micron resolution. For patterns having multiple fracture sets or other variability, the procedure should also be capable of easily separating digitized fractures into subsets on the basis of fracture type (Laubach, 1997) and other criteria such as orientation (Gomez et al., 2003). For our goal of scaling analysis (i.e. Marrett et al., 1999; Ortega and Marrett, 2000), we also need to look at both scanline (1-D) and area (2-D) samples. Currently, automated fracture picking from SEM-CL images is not feasible owing to the complexity of gray-scale textures of pores, grains and cements versus those from fractures. Finally, we sought digitizing and spreadsheet software that is readily available. Quantifying and plotting fracture attributes in familiar spreadsheet software means that adding new types of analysis or displays is straightforward.

3.1. Fracture mapping

Although any graphic software that allows image scale calibration and coordinate export would be adequate to map fractures, we selected Didger® 3 because it allows us to assign an ID to each drawn object. This ID can be used later to separate fractures into subsets having the same classification (e.g. transgranular or intragranular; Gomez et al., 2003). If the digitizing software does not have this capability, each fracture type can be mapped independently (each one in a different file), but doing so makes the process slower.

The following is our procedure for mapping fractures present on an image mosaic:

(i) Import image mosaic into the digitizing software.
(ii) Calibrate the image mosaic. Calibration commonly involves locating a coordinate origin and assigning a length scale (e.g. pixels per millimeter) in both *X* and *Y* directions using a line of known length as a guide.
(iii) Draw the scanline (1-D analysis) or the area (2-D analysis) of the image mosaic where fractures are going to be mapped.
(iv) Digitize each fracture with a closed polygon composed of four anchor points. The first and third points should always represent the fracture tips. The second and fourth points must represent the aperture (Fig. 5). If wanted, assign an ID (fracture type) to each fracture. If a fracture extents beyond the width of the image mosaic, the fracture tip would be represented by the intersection of the fracture with the image boundaries (Fig. 5) and the length of that particular fracture would be censored.

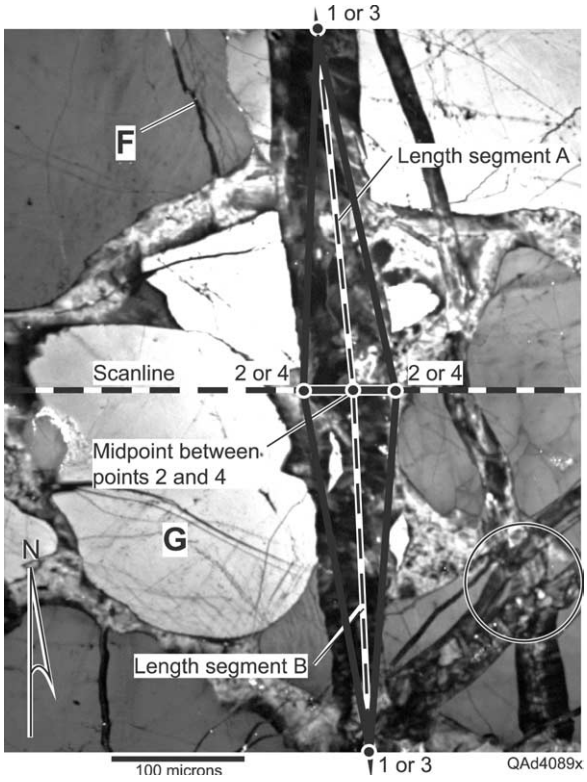

Fig. 5. Fracture mapping convention. Diagram shows fracture aperture measured along scanline (dashed line). Background is bedding-parallel CL image, Cambrian Eriboll Formation sandstone. Note that in this example, fracture length is severely censored owing to fracture tips extending outside image area. G, grain; F, quartz-filled fractures. Circle shows north-striking fracture crosscut by two northeast-striking fractures.

(v) Export coordinates of the four points of all fractures (leftmost fracture on Fig. 6) in a format that can be easily read by spreadsheet software, say Excel®.

Although there are some commercial digitizing programs that, once calibrated, can quantify length or angles of drawn objects, we prefer to calculate fracture attributes in a spreadsheet instead of within the digitizing program to keep control of how those attributes are calculated and displayed. It also gives us the ability to compile and display attributes of fracture subsets and to generate many kinds of diagrams, including cumulative frequency diagrams of fracture attributes like aperture or length. Spreadsheets also allow calculation of distances between digitized objects, in this case fracture spacing (Gomez, 2004).

For 1-D quantification of fracture attributes, the aperture of a fracture is the distance between the two walls along the scanline (Marrett et al., 1999). In a 2-D study, the aperture is the distance between fracture walls measured at its largest value. In our method, there are four possible ways that a fracture can be digitized with four points (Fig. 6); any of them would be adequate, as long as points 1 and 3 are located on the fracture tips, and points 2 and 4 are used to measure fracture aperture.

When all fractures are mapped, their IDs and the coordinates of the points that define them can be exported in a format that

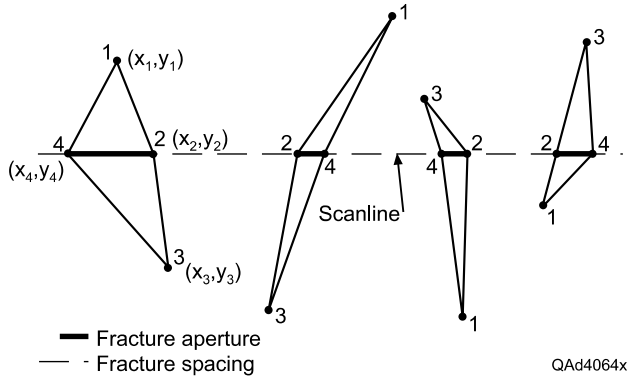

Fig. 6. Fracture aperture and spacing measured along a scanline and mapping protocol showing four possible ways a fracture can be digitized with four points. In our method, any of them would be adequate, as long as points 2 and 4 are located along the scanline (used to measure aperture) and points 1 and 3 represent the fracture tips. With our software, if the four points that define a fracture are digitized in the wrong order, all values of fracture properties will be wrong.

can be read by spreadsheet software (we used Excel®). Didger® 3 can export coordinates in a file format called Atlas Boundary format (BNA). Atlas Boundary files are ASCII format files that contain the coordinates of polygons, points or lines and their corresponding IDs. Although we selected a specific file format for transferring coordinates and IDs of fracture objects to a spreadsheet, any format is adequate, provided that the exported data is transformed into a BNA-equivalent format before is imported into the spreadsheet.

3.2. Quantification of fracture attributes

Although fracture quantification was greatly facilitated by in-house software written in C++ (Ortega, 2002), this program was linked to commercial software that became obsolete. The new GoMezure™ template, on the other hand, uses a common platform. One advantage of using spreadsheet software instead of in-house software specifically written (using a programming language such as C++) is that in a spreadsheet, equations are visible and variables of those equations are easily traceable by—instead of invisible to—the user.

The GoMezure™ spreadsheet template was designed to quantify fracture length, strike, aperture, and spacing, and calculates fracture length-weighted strike and fracture strain. In addition, GoMezure™ can generate displays or calculate descriptive statistics (e.g. arithmetic mean) of fracture attributes for all digitized fractures or for a group of fractures having a common identity. GoMezure™ is organized in worksheets (individual spreadsheet of an Excel® file), with each worksheet designed to quantify and display a particular fracture attribute.

One worksheet is exclusively dedicated to receiving input from digitizing software. Fracture attributes are calculated and compiled, and *mapping* errors are identified and flagged. We programmed GoMezure™ cells where tests are performed to change color and to write a descriptive message briefly explaining why a test failed. The data-quality tests performed in GoMezure™ include checking that all fractures are digitized using only four points (Fig. 5), verifying that four points that represent each fracture are digitized in the proper order (Fig. 6) by comparing fracture length and fracture aperture (typically, transgranular fracture length is much greater than fracture aperture), and verifying that the scanline length or area of study is entered. One of these two last values must be present if cumulative frequency distributions are to be generated.

The advantage of representing fractures as four-point polygons is that fracture attributes can be reduced to distances between points (e.g. length, aperture) and angles (strike). These distances or angles can easily be calculated using trigonometric calculations. For instance, using the Pythagorean Theorem, fracture aperture can be calculated as follows (leftmost fracture, Fig. 6):

$$\text{Fracture aperture} = \sqrt{(X_2 - X_4)^2 + (Y_2 - Y_4)^2} \quad (1)$$

Although 1-D scanlines are biased against oblique fractures, if azimuth of an individual fracture is not perpendicular to the azimuth of the 1-D scanline, the aperture measured is an apparent aperture. True apertures could be recovered using a trigonometric correction (Terzaghi, 1965) incorporated in GoMezure™.

Ortega (2002) calculated fracture length as half the perimeter of the digitized four-point polygon. However, this calculation is reliable only when the aperture of a fracture is several times smaller than its length, which may not be the case for 1-D analysis because narrow mosaics censor fracture lengths close to and larger than the width of the image mosaic. Alternatively, we calculate fracture length as the distance between point 1 and the midpoint between points 2 and 4 (segment A of Fig. 5), plus distance between point 3 and the midpoint between points 2 and 4 (segment B of Fig. 5).

The strike of an individual fracture can be calculated as the azimuth of a line joining points at the tips of a fracture (Ortega, 2002). To preserve more information and to account for curved fractures, we calculate instead the azimuth of an individual fracture as a length-weighted azimuth of segments A and B (Fig. 5). Because geographic north could be located in any direction, the strike of an individual fracture is calculated with respect to a hypothetical north located toward positive values along the *Y* axis. If the orientation of the thin section is known, it will be possible to calculate the true strike of all digitized fractures.

Rose diagrams of strike of the entire fracture population or a subset are calculated using circular statistics. The visual quality of rose diagrams from our spreadsheet software is satisfactory for on-screen analysis. If a more appealing rose diagram or any other kind of fracture orientation diagram is needed, all the values of fracture strike can be extracted easily. Using petrographic or CL images, we need mutually orthogonal thin sections to specify fracture dip in addition to fracture strike.

To avoid imposing limitations on the order in which individual fractures are digitized, the initial step to calculate fracture spacing along a scanline is to sort all fractures in decreasing value of the *X* coordinate of point 2 (Figs. 5 and 6).

The next step is a nested conditional statement for calculating fracture spacing (distance between nearest-neighbor fractures), regardless of which of the four possible ways of digitizing a fracture is used (Fig. 6).

Cumulative frequency distributions of fracture attributes are commonly used to quantify properties of a fracture network (Marrett et al., 1999; Gillespie et al., 2001; Gale et al., 2004). However, when the number of fractures is great and their classification is intricate (sets organized by strike, aperture, type of crystalline cement, etc.), the analyst is faced with the time-consuming task of creating individual cumulative frequency distributions for each set of fractures. The method presented here automates creation and display of cumulative frequency distributions for as many as four individual fracture sets or up to three combined fracture sets. We analyze cumulative frequency rather than cumulative number because doing so allows comparison of data sets collected at different scales or predictions of fracture attributes across a wide range of scales (Marrett et al., 1999; Ortega and Marrett, 2000).

Most spreadsheets, including Excel®, can group calculations and tasks into scripts, called *macros*, which can be executed without having to execute the tasks individually. The following are tasks recorded in all macros designed to generate cumulative frequency distributions of fracture attributes:

(i) Copy from the first worksheet (where attributes for each fracture are calculated and compiled) values of the fracture attribute to be studied and respective primary ID for all fractures.
(ii) If the primary ID of a fracture matches criteria entered by the user, then copy the value of the fracture attribute to the next column.
(iii) Sort the output from step (ii) from largest to smallest. In a contiguous column, starting with a value of one, assign increasing numbers (increments of one) to the fractures. This value is called cumulative number, which indicates how many fractures have an attribute equal to or larger than the corresponding value of fracture attribute.
(iv) From sorted values of fracture attribute, copy values of the fracture attribute that are not duplicates and their corresponding cumulative numbers to the next two columns. For fractures with duplicated fracture attributes only the one with the largest cumulative number should be copied.
(v) In an additional column, divide the consecutive number (for the values of fracture attribute that are not duplicates) by the length of the scanline (1-D analysis) or the area (2-D analysis) of the image where fractures were digitized. The resulting value is the cumulative frequency.

Although retention of duplicate values of fracture attributes would not significantly affect the appearance of a cumulative frequency distribution, it is required for an accurate calculation of the equation of a probability distribution (e.g. negative exponential). To study subsets of the data, we use conditional statements prior to sorting the data (step (iii)) to select fractures of the same type on the basis of classifications applied during mapping. Fractures can also be segregated by user-defined ranges of strike.

4. Examples: fractures in NE Mexico and NW Scotland

4.1. Dolostone—petrographic images

The Monterrey Salient of the Sierra Madre Oriental of Mexico has large outcrops of the Lower Cretaceous Cupido Formation (Goldhammer, 1999). Excellent exposure, together with abundant fractures, makes the Cupido Formation a good place to test analytical techniques (Marrett et al., 2004; Ortega et al., 2006), and to study the attributes of natural fractures (e.g. spatial arrangement; Gomez, 2004). In the Cupido Formation, fractures are abundant in dolostone layers and may have formed prior to regional folding (Marrett and Laubach, 2001; Ortega, 2002). Our test sample is from one of these dolostones. Fractures are filled mainly by crystalline calcite that contrasts with the dolomitic rock mass such that most microfractures are visible using a transmitted-light microscope.

Macroscopically visible fractures and microfractures are present in a large (320×350×70 mm) sample that covers most of a fracture cluster (Fig. 3). The sample was cut into seven contiguous thin sections, 50×75 mm in size (Fig. 3). From these samples, a long (194 images) and narrow (1 image) digital mosaic at a magnification of 50× was acquired using a petrographic microscope. The aperture and spacing between 712 fractures were measured on a 277-mm-long scanline crossing the short dimensions of the rectangular thin sections. Although the scanline length on each thin section is about the same size, the heterogeneity in spatial arrangement of fractures causes individual thin sections to have different numbers of microfractures along the scanline (between 51 and 147 fractures).

The cumulative frequency of fracture aperture of one of those seven thin sections extends for about 3 orders of magnitude of aperture and does not display a common power-law distribution with the population of genetically related macrofractures measured in outcrop (Fig. 7a). In contrast, cumulative frequency of microfractures measured on the seven contiguous thin sections varies over 4.5 orders of magnitude of fracture aperture—a large range compared with published aperture distributions (Marrett et al., 1999)—and shows a power-law scaling over 2 orders of magnitude (Fig. 7b). Typically an increase in number of fractures corresponds with an increase in range of fracture property values. In contrast to the microfracture population for a single thin section, the microfracture population from the seven thin sections (entire sample) displays a common power-law distribution with the macrofractures measured in outcrop (Fig. 7b).

By providing a scanline larger than a single thin section, we obtained a representative population of the microfractures, which allowed us to quantify the size and spacing of microfractures in a way that would not be apparent from a sample of smaller size (Fig. 7b and c). In addition, only a scanline larger than a single thin section would have allowed us

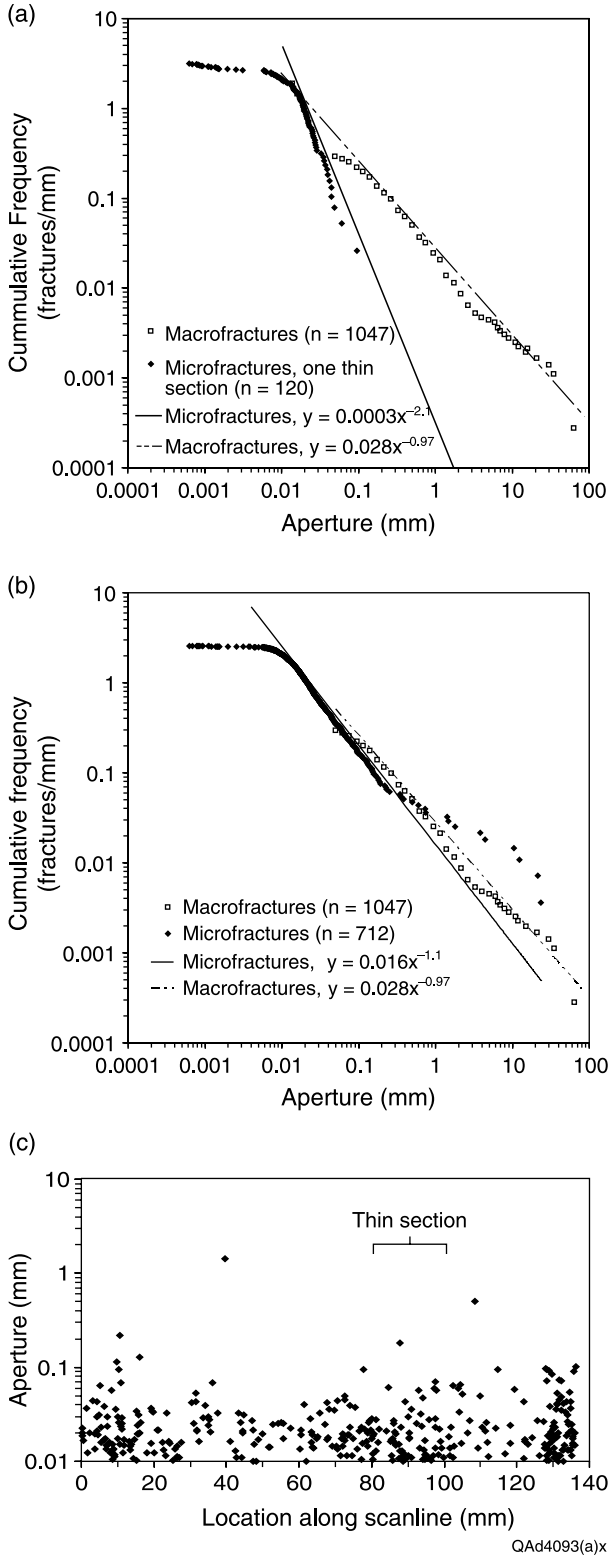

Fig. 7. Fracture attributes of sample from Cupido dolostone, NE Mexico. (a) Cumulative frequency distribution of fracture aperture for only one of the seven contiguous thin sections. Also shown are macrofractures and a power-law regression to the macrofracture population. Microfractures and macrofractures do not share a similar aperture distribution. (b) Cumulative frequency distribution of fracture aperture for seven consecutive thin sections having no gaps between them. Microfractures display a power-law scaling over 2 orders of magnitude (0.01–1 mm). Also shown are macrofractures and separate power-law regressions to micro- and macrofracture populations. Micro- and macrofractures can be described by similar power-laws. We interpret deviation of apertures below 0.01 mm from power-law to be a truncation artifact. (c) Aperture versus location for microfractures along four of the seven contiguous thin sections (scanline of 135 mm). Note the variation in the fracture intensity along the scanline; a noticeable increase in fracture intensity corresponds to a microfracture cluster (5–15, 65–100, and 128–135 mm).

to use the cumulative frequency distribution of microfracture aperture to predict the intensity of genetically related macrofractures (Marrett et al., 1999; Ortega et al., 2006). For instance, a single thin section inside one microfracture cluster (60–95 mm; Fig. 7c) would have overestimated the fracture intensity of the entire microfracture population and the clustering of the microfracture population would have remained undetected. Owing to the scale of non-random fracture clustering, quantitative spacing analysis of this microfracture population successfully predicted some characteristics of the spatial arrangement of genetically related macrofractures (Gomez, 2004).

4.2. Sandstone—SEM-CL images

As part of an ongoing fracture and diagenesis study (Diaz-Tushman et al., 2005), we have extensively sampled Cambrian Eriboll Sandstone in the footwall of the Moine thrust zone in northwestern Scotland (Strachan et al., 2002). The rock is quartz cemented, has very low porosity, a grain size of about 100 μm, and contains numerous quartz-filled opening-mode microfractures only partly visible petrographically as fluid-inclusion planes. We selected a 20-cm-long sample from a tilted but otherwise structureless bed for testing our method. We focus on a bed-parallel mosaic and scanline oriented normal to one of the fracture sets in this sample. We used the method outlined in Section 2.1 to collect four 25×46 mm thin sections having no gaps between them (Fig. 2). The scanline followed the long dimension of the thin sections (Fig. 4). Microfractures are parallel to macrofractures, and both are arranged in two sets having distinct orientations regionally (Figs. 1b and 5).

The 138.5-mm-long mosaic consists of 191 pairs of registered panchromatic CL and SEI images collected in automated mode (Fig. 4). The scanline intersected 2095 microfractures, 325 of which are transgranular (Gomez et al., 2003) and therefore more reliable guides to the attributes of genetically related macrofractures (Laubach, 1997). Individual thin sections display 346, 413, 660, and 676 microfractures of which 61, 62, 105, and 97 are transgranular, respectively.

Microfracture strike has been used to correctly predict the strike of genetically related macrofractures (Laubach, 1997; Ortega and Marrett, 2000). A diagram of microfracture strike for transgranular and intragranular microfractures in one of the four thin sections that compose the entire scanline displays only one preferred orientation (Fig. 8a). In contrast, transgranular and intragranular microfractures from all four thin sections have two distinct preferred orientation maxima (Fig. 8b). Two directions are also present in the subset of only transgranular microfractures for all four thin sections

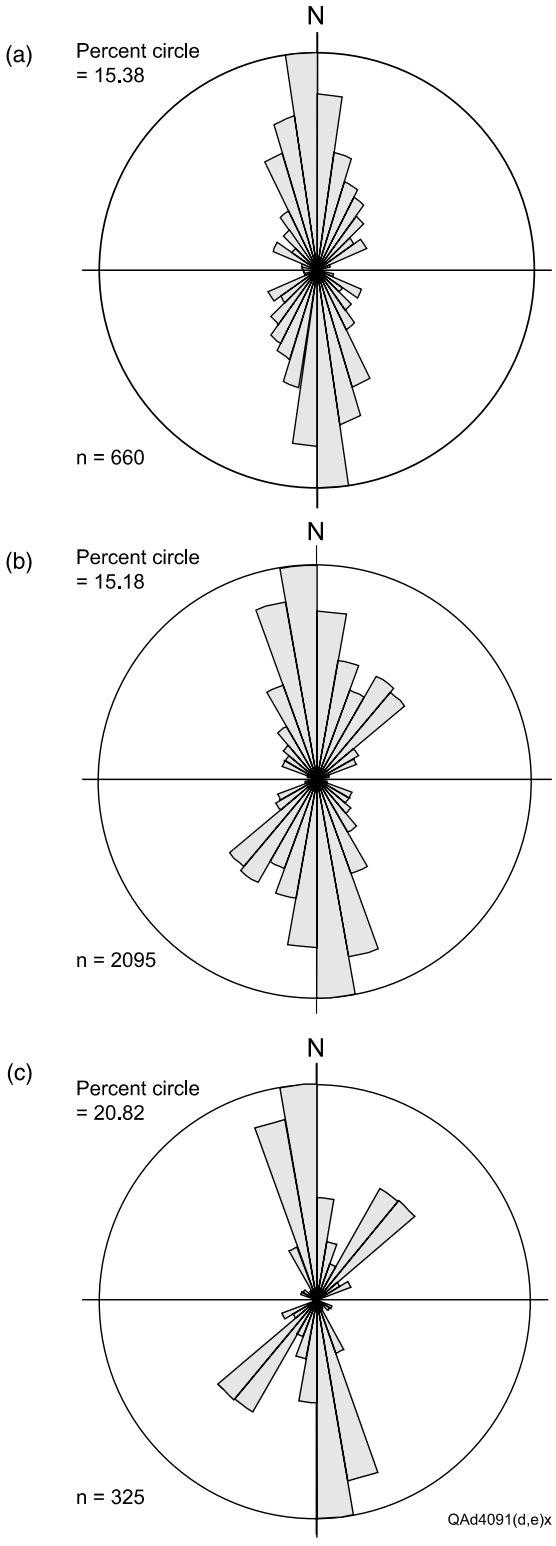

Fig. 8. Length-weighted, equal-angle rose diagrams of microfracture strike collected along a scanline; quartz-sealed microfractures; Cambrian Eriboll Formation sandstone, Scotland. (a) Transgranular and intragranular fractures, scanned-CL mosaic, 37 mm long from one thin section. (b) Transgranular and intragranular fractures, scanned-CL mosaic, 138.5-mm-long continuous sample, four thin sections. (c) Transgranular fractures only, scanned-CL mosaic, 138.5-mm-long continuous sample, four thin sections. North- and northeast-striking preferred orientations of these two sets differ in strike by about 50°. Crosscutting relations indicate that the north-striking set is older.

(Fig. 8c), and this pattern matches that of macroscopic fractures in outcrop.

The scanline we drew along the center of the image mosaic intersected 2095 microfractures, which ranged in aperture from 0.00031 to 0.98 mm (Fig. 9). Cumulative apertures along the scanline record strain of 4.9%. Microfracture strain measurements using SEM-CL have greater accuracy than would be possible using cold-cathode CL methods because the resolution of SEM-CL reveals more small fractures more clearly and these small fractures represent much of the rock's deformation. CL results are far more accurate than strain estimates from fluid-inclusion size (Onash, 1990), because CL shows that fluid-inclusion diameter is commonly much smaller than aperture and not a good proxy for fracture width.

The large size of the image mosaic and the numerous fractures, together with the flexibility of the spreadsheet software, allows rapid, systematic description of all or part of the fracture population. The shape of the image mosaic results in severe censoring of fracture lengths above 0.65 mm, which is about the width of an individual CL image at 150× (Fig. 5). We therefore focused on analysis of kinematic apertures of fractures and spatial arrangement of those fractures.

Inspection of the image mosaic shows that there are many more small microfractures than large (Fig. 4). Cumulative frequency plots of aperture show evidence of power-law scaling, particularly in the transgranular fracture population (Fig. 9a and b). The population that includes all microfractures shows two slopes (Fig. 9b), which may result from mixing of fracture populations, including inherited fractures (Laubach, 1997). Separating transgranular fractures produces a population that is well fit by a power-law across approximately 2 orders of magnitude, but further subdividing this population by strike gives a result that is geologically more meaningful (Fig. 9a and b). We know from crosscutting relations, after all, that transgranular fractures compose two sets that formed at different times and have different orientations (Figs. 1b and 5). However, in one of the thin sections there are only eight microfractures with a northeastward strike; not enough fractures to generate a reliable distribution (Fig. 9a). In contrast, a scanline that spanned four contiguous thin sections detected 48 microfractures with the same northeastward strike; a stronger signal of the true fracture pattern (Fig. 9b).

Unraveling the intriguing patterns in these plots is beyond the scope of this paper. Mapping and manipulating the measurements of a population of more than 2000 fractures allows us to explore these patterns efficiently. For instance, the pattern of the combined strike and type population may differ in fracture intensity, as defined by cumulative frequency of aperture (Fig. 9b), yet the two sets are similar in length to aperture ratio (Fig. 9c).

Key evidence for fracture attributes, including numbers of fracture sets, strike, crosscutting relations, strain, the volume of cement sequestered in microfractures, and meaningful data on microfracture population statistics are only fully manifest at scales larger than a single thin section. For example, plots of aperture versus distance along scanline show qualitative evidence of fracture clustering (Fig. 9d). The clustering pattern

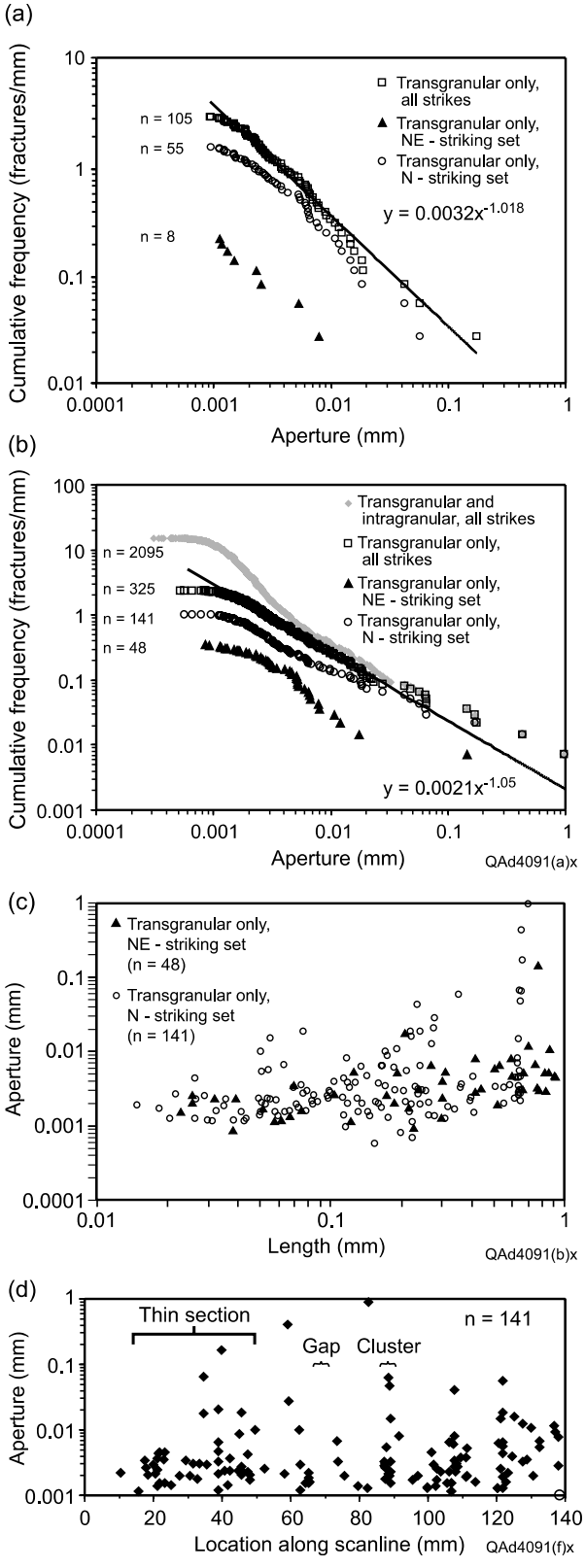

Fig. 9. Fracture attributes, Eriboll Formation sandstone, NW Scotland sample. (a) Cumulative frequency, fracture aperture from one thin section. Curves show microfracture population for transgranular fractures only subdivided by strike (all strikes, NE-striking, 30–50°, and N-striking, 160–190°). North-striking set is older, judging by crosscutting relations. Regression is power-law for transgranular microfractures only, all strikes. (b) Cumulative frequency, fracture aperture for four thin sections. Curves show microfracture population subdivided by fracture type (transgranular versus transgranular and intragranular fractures combined) and/or strike (NE-striking, 30–50°, and N-striking, 160–190°). Transgranular and intragranular fractures of all strikes show two slopes. (c) Aperture versus length, transgranular fractures of N- and NE-striking sets. (d) Aperture versus location of one set of transgranular fractures along scanline; 138.5-mm-long continuous sample; open circle marks end of scanline. Note gaps at 25, 55, 70, 93, and 117 mm and clusters at 20, 40, 65, 108, and 123 mm (two are labeled).

would not be evident without a scanline that extended beyond a single thin section. This data set also illustrates why the method to generate consecutive thin sections without gaps between them is needed for microfracture-spacing analysis. No data zones (gaps) would corrupt spacing data beyond the first kerf, and with every additional gap the error in fracture spacing data would increase (Fig. 9d).

5. Discussion

Although an issue in many types of textural and crystallographic studies (e.g. Trimby and Prior, 1999), the advantages of texture studies over wide sample areas are well illustrated by studies of fault rocks, where most published observations are restricted to image areas smaller than a thin section despite fault rock heterogeneities that extend over larger scales (e.g. Sammis et al., 1987; Biegel et al., 1989; Marone and Scholz, 1989). All these studies of structural fabrics in thin sections were limited by the largest magnification of the tool(s) selected and assuming there was no limit on the size of sample; these studies were also bounded by the size sample that they could image. Some studies are restricted to individual images at different magnifications (Marone and Scholz, 1989) while others used 1-D (Biegel et al., 1989) or 2-D (Sammis et al., 1987) mosaics but always without exceeding the rock sample available in a single thin section. Because fault fabrics are to some extent penetrative, even individual images provide some information. The same is not true for many fracture populations, where individual fractures are distributed throughout the rock.

Because of the distributed character of microfractures, there is no guarantee that an individual microscopic image or an image mosaic with one dimension as long as an individual thin section will have a large enough population to meaningfully quantify the population attributes. Many rocks have a lower overall fracture intensity than samples illustrated in this paper or in Marrett et al. (1999). For example, in a study of microfracture intensity in Cretaceous sandstones, Gomez et al. (2003) found that it was only possible to obtain a meaningful population (87 transgranular microfractures detected in about 110 mm of SEM-CL scanline) that accurately predicted macrofracture intensity in a horizontal core by combining transgranular microfractures detected in image mosaics from five separate thin sections.

The rocks of Gross and Engelder (1995) and Gomez et al. (2003) have about 90 and 63% lower transgranular microfracture intensity, respectively, than the Eriboll Sandstone samples described in Section 4.2 (Fig. 9b). Although intensely fractured, Eriboll Sandstone samples required

a scanline larger than an individual thin section to detect the two sets of transgranular fractures having distinct orientation maxima (Fig. 8b and c) and microfracture clustering (Fig. 9d). We expect that the larger microfracture populations that could be obtained from samples larger than an individual thin section would better define the aperture distributions of the rocks studied by Gross and Engelder (1995) and Gomez et al. (2003).

Although it is possible to increase the number of fracture measurements from a single thin section by using serial parallel scanlines, it is likely that many fractures in the thin section would intersect more than one scanline. Multiple measurements of some fractures produce artifacts that can only be explicitly accounted for by understanding aperture variations with fracture length, which is neither simple nor consistent (Moros, 1999). Of course if multiple orientation sets are present, then additional scanlines may be needed.

Image areas of square centimeters are needed to measure microfracture populations effectively in many slightly deformed rocks. A prohibitively large amount of time—days of imaging time—is required to manually acquire even 1-D image mosaic strips having lengths in centimeters at 150×. Yet for many applications, large rectangular (2-D) mosaics are preferable, for example, because of bias in fracture orientation statistics and censoring of fracture lengths in 1-D image strips. The methods presented here largely overcome these challenges.

A key step in the overall process is automation of image collection and stitching. The procedure we describe uses about 75% less SEM-operator time than manual SEM image collection for the same amount of machine time. We can generate SEM-based mosaics of paired-CL and SEI images at a rate of about 3.5 min/mm of scanline at 150×. Nevertheless, the CL mosaics we describe cover only about 2% of the area we desire to image. Our longest SEM-CL mosaic imaged less than 1 cm^2 ($<89\ mm^2$). This area is reasonable for 1-D microfracture analysis, but for 2-D analysis, larger image areas are needed that use a greater percentage of the sample. On the other hand, we have not yet fully exploited the capabilities of commercially available automation software. Further improvements in the rate-limiting step of CL image acquisition will undoubtedly allow us to accomplish 2-D imaging of thin-section scale areas.

New software greatly improves the efficiency of mapping, data reduction, and display of structural fabric data. Together, image automation and these efficiencies in data reduction allow us to use much larger samples, which in turn provide much richer microfracture data sets. Using the new method to create continuous samples larger than one thin section, we were able to document fracture population patterns that would not have been apparent in a smaller sample. The same method can be used successfully, regardless of rock type, on mosaic images from scanned-CL or petrographic microscopes. These improvements over manual methods make systematic documentation and quantification of microfracture fabrics in many rocks practical.

6. Conclusions

Microfractures have been used to estimate the orientation and spatial arrangement of genetically related macrofractures. Microfractures that follow a power-law distribution of sizes have also been used to estimate the intensity of macrofractures that can control fluid flow but that are commonly challenging to sample in the subsurface. For these types of analyses, large populations of microfractures are vital. Effective methods of measuring fossilized microfracture systems therefore have utility in structural analysis.

Microfracture populations contain much information that is only fully manifest at scales larger than a single thin section. This makes rapid digital imaging and quantification vital for analysis of such populations. We show that in examples from two different lithologies (dolostone and sandstone) using different types of microscopic images (petrographic and SEM-CL, respectively), this approach provides key evidence for numbers of sets, strike, crosscutting relations, strain, the volume of microfracture-sequestered cement, and meaningful data on microfracture population size and spacing patterns that would not be evident otherwise.

Acknowledgements

Supported by a grant from the Chemical Sciences, Geosciences and Biosciences Division, Office of Basic Energy Sciences, Office of Science, U.S. Department of Energy, and by industrial associates of the Fracture Research and Application Consortium. We are grateful to the Geology Foundation, Jackson School of Geosciences, for support of fieldwork in Mexico (Ronald K. DeFord Field Scholarship, Gomez) and in Scotland (Jackson Research Fellowship, Laubach), acquisition of SEM automation software, and contributions to color figure costs. Additional support for sampling in Mexico was provided by a Graduate Student Research Grant from the Geological Society of America (Gomez). John Hooker and Julia Gale tested and suggested improvements to GoMezure™. We thank Robert Reed and Kitty Milliken for leading our effort to automate SEM-CL image acquisition and Orlando Ortega for starting us on the road to digital quantification of microfractures. Randall Marrett indulged us with many clarifications about the topology of fracture populations. We appreciate comments from K. Milliken, S. Mosher, D. Wiltschko and an anonymous reviewer.

References

Biegel, R.L., Sammis, C.G., Dieterich, J.H., 1989. The frictional properties of a simulated gouge having a fractal particle distribution. Journal of Structural Geology 11, 827–846.

Diaz-Tushman, K., Laubach, S.E., Gomez, L.A., 2005. Expanding the tectonic history of the highlands: a strain study utilizing fractures from Cambrian Eriboll Group Sandstones (abs.). Geological Society of America Abstracts with Programs 37 (7), 235.

Gale, J.F.W., Laubach, S.E., Marrett, R.A., Olson, J.E., Holder, J., Reed, R.M., 2004. Predicting and characterizing fractures in dolostone reservoirs: using the link between diagenesis and fracturing. In: Braithwaite, C.J.R.,

Rizzi, G., Darke, G. (Eds.), The Geometry and Petrogenesis of Dolomite Hydrocarbon Reservoirs. Geological Society, London, Special Publications 235, pp. 177–192.

Gillespie, P.A., Walsh, J.J., Watterson, J., Bonson, C.G., Manzocchi, T., 2001. Scaling relationships of joint and vein arrays from The Burren, Co. Clare, Ireland. Journal of Structural Geology 23, 183–201.

Goldhammer, R.K., 1999. Mesozoic sequence stratigraphy and paleogeographic evolution of northeast Mexico. In: Bartolini, C., Wilson, J.L., Lawton, T.F. (Eds.), Mesozoic Sedimentary and Tectonic History of North-Central Mexico. Geological Society of America, Special Paper 340, pp. 1–58.

Gomez, L., 2004. Predicting macrofracture spatial arrangement from small rock samples: testing new analytical techniques using microfracture spacing (abs). AAPG Annual Convention Official Program, Dallas A53.

Gomez, L., Gale, J., Laubach, S., Cumella, S., 2003. Quantifying Fracture Intensity: an Example from the Piceance Basin 2003. Rocky Mountain Association of Geologists Piceance Guidebook, on CD.

Gross, M., Engelder, T., 1995. Strain accommodated by brittle failure in adjacent units of the Monterrey Formation, U.S.A.: scale effects and evidence for uniform displacement boundary conditions. Journal of Structural Geology 17, 1303–1318.

Kearsley, A., Wright, P., 1988. Geological applications of scanning electron cathodoluminescence imagery. Microscopy and Analysis September, 49–51.

Kranz, R.L., 1983. Microcracks in rock: a review. Tectonophysics 100, 449–480.

Laubach, S.E., 1989. Paleostress directions from the preferred orientation of closed microfractures (fluid-inclusion planes) in sandstone, East Texas basin, U.S.A. Journal of Structural Geology 11, 603–611.

Laubach, S.E., 1997. A method to detect natural fracture strike in sandstones. American Association of Petroleum Geologists Bulletin 81, 604–623.

Laubach, S.E., 2003. Practical approaches to identifying sealed and open fractures. American Association of Petroleum Geologists Bulletin 87, 561–579.

Laubach, S.E., Reed, R.M., Olson, J.E., Lander, R.H., Bonnell, L.M., 2004. Coevolution of crack-seal texture and fracture porosity in sedimentary rocks: cathodoluminescence observations of regional fractures. Journal of Structural Geology 26, 967–982.

Lespinasse, M., 1999. Are fluid inclusion planes useful in structural geology? Journal of Structural Geology 21, 1237–1243.

Marone, C., Scholz, C.H., 1989. Particle size-distribution and microstructures within simulated fault gouge. Journal of Structural Geology 17, 799–814.

Marrett, R., 1996. Aggregate properties of fracture populations. Journal of Structural Geology 18, 169–178.

Marrett, R., Laubach, S.E., 2001. Fracturing during burial diagenesis. In: Marrett, R. (Ed.), Genesis and Controls of Reservoir-Scale Carbonate Deformation, Monterrey Salient, Mexico The University of Texas at Austin, Bureau of Economic Geology, Guidebook 28, pp. 109–120.

Marrett, R., Ortega, O., Kelsey, C., 1999. Extent of power-law scaling for natural fractures in rock. Geology 27, 722–802.

Marrett, R., Gale, J., Gomez, L., 2004. New techniques for characterizing fracture spacing: examples from Northeastern Mexico and Central Texas (abs.). AAPG Annual Convention Official Program, Dallas A91.

Milliken, K.L., Laubach, S.E., 2000. Brittle deformation in sandstone diagenesis as revealed by scanned cathodoluminescence imaging with application to characterization of fractured reservoirs. In: Pagel, M., Barbin, V., Blanc, P., Ohnenstetter, D. (Eds.), Cathodoluminescence in Geoscience. Springer, Berlin, pp. 225–243.

Moros, J.G., 1999. Relationship between fracture aperture and length in sedimentary rocks. M.Sc. thesis, The University of Texas at Austin.

Onash, C.M., 1990. Microfractures and their role in deformation of a quartz arenite from the central Appalachian foreland. Journal of Structural Geology 12, 883–894.

Ortega, O., 2002. Fracture-size scaling and stratigraphic controls on fracture intensity. Ph.D. dissertation, The University of Texas at Austin.

Ortega, O., Marrett, R., 2000. Prediction of macrofracture properties using microfracture information, Mesaverde group sandstones, San Juan Basin, New Mexico. Journal of Structural Geology 22, 571–588.

Ortega, O., Marrett, R., Laubach, S.E., 2006. A scale-independent approach to fracture intensity and average spacing measurement. American Association of Petroleum Geologists Bulletin 90, 193–208.

Pagel, M., Barbin, V., Blanc, P., Ohnenstetter, D. (Eds.), 2000. Cathodoluminescence in Geosciences. Springer, Berlin.

Passchier, C.W., Trouw, R.A.J., 1998. Microtectonics. Springer, Berlin.

Sammis, C.G., King, G., Biegel, R.L., 1987. The kinematics of gouge deformation. PAGEOPH 125, 777–812.

Strachan, R.A., Smith, M., Harris, A.L., Fettes, D.J., 2002. The northern Highland and Grampian terranes. In: Trewin, N.H. (Ed.), The Geology of Scotland. The Geological Society, London, pp. 81–148.

Terzaghi, R.D., 1965. Sources of error in joint surveys. Geotechnique 15, 287–304.

Trimby, P.W., Prior, D.J., 1999. Microstructural imaging techniques: a comparison between light and scanning electron microscopy. Tectonophysics 303, 71–81.

van Daalen, M., Heilbronner, R., Kunze, K., 1999. Orientation analysis of localized shear deformation in quartz fibres at the brittle–ductile transition. Tectonophysics 303, 83–107.